ARTICLE

Activation of NMDA receptors and the mechanism of inhibition by ifenprodil

Nami Tajima[1], Erkan Karakas[1], Timothy Grant[2], Noriko Simorowski[1], Ruben Diaz-Avalos[2], Nikolaus Grigorieff[2] & Hiro Furukawa[1]

The physiology of *N*-methyl-D-aspartate (NMDA) receptors is fundamental to brain development and function. NMDA receptors are ionotropic glutamate receptors that function as heterotetramers composed mainly of GluN1 and GluN2 subunits. Activation of NMDA receptors requires binding of neurotransmitter agonists to a ligand–binding domain (LBD) and structural rearrangement of an amino-terminal domain (ATD). Recent crystal structures of GluN1–GluN2B NMDA receptors bound to agonists and an allosteric inhibitor, ifenprodil, represent the allosterically inhibited state. However, how the ATD and LBD move to activate the NMDA receptor ion channel remains unclear. Here we applied X-ray crystallography, single-particle electron cryomicroscopy and electrophysiology to rat NMDA receptors to show that, in the absence of ifenprodil, the bi-lobed structure of GluN2 ATD adopts an open conformation accompanied by rearrangement of the GluN1–GluN2 ATD heterodimeric interface, altering subunit orientation in the ATD and LBD and forming an active receptor conformation that gates the ion channel.

NMDA receptors are critically involved in brain development and function, including learning and memory formation. NMDA receptors belong to the family of ionotropic glutamate receptors, which are glutamate-gated ion channels comprised of three major families, α-amino-3-hydroxy-5-methyl-4-isoxazole propionic acid (AMPA) (GluA1–4), kainate (GluK1–5), and NMDA receptors (GluN1, GluN2A–D, and GluN3A, B)[1]. NMDA receptors are obligatory heterotetramers mainly composed of two copies each of the GluN1 and GluN2 subunits, which bind glycine and L-glutamate, respectively. Under physiological conditions, the opening of the NMDA receptor ion channel requires concurrent binding of glycine and L-glutamate[2–4], and relief of magnesium block at the ion channel pore by membrane depolarization[5,6]. The resulting calcium flux[7] triggers a cascade of signal transduction necessary for synaptic plasticity[8]. Dysfunctional NMDA receptors are implicated in various neurological diseases and disorders such as Alzheimer's disease, depression, stroke, epilepsy and schizophrenia[1,9].

NMDA receptor subunits, like those of other ionotropic glutamate receptor family members, are composed of multiple domains including an ATD, LBD, transmembrane domain (TMD) and carboxy-terminal domain (CTD) (Extended Data Fig. 1). Binding of neurotransmitter agonists to the LBD produces a large conformational change involving closure of the bi-lobed structure that is required for ion channel gating in all ionotropic glutamate receptors[10–12], but a distinctive feature of NMDA receptors is that activity is also robustly regulated by the ATD[13]. For example, the ATD controls the open probability and speed of deactivation[14,15], and binds allosteric modulator compounds to regulate ion channel activity[16]. In contrast to NMDA receptors, there is no apparent role for the ATDs of AMPA and kainate receptors[17–20] in regulating the ion channel activities, even though they are essential for subunit assembly[21]. The recent crystal structures of intact heterotetrameric GluN1–GluN2B NMDA receptors complexed with agonists and allosteric inhibitors, ifenprodil or Ro 25-6981, revealed that the ATD and LBD interact tightly via a large interface area, unlike GluA2 AMPA receptor and GluK2 kainate receptor whose ATDs and LBDs interact minimally[17,20,22,23], implying that activation of NMDA receptors requires concerted conformational alterations in the ATD and LBD[19,22,23]. The structures of the intact GluN1–GluN2B NMDA receptors[22,23] and of the isolated ATDs complexed to ifenprodil[24] or zinc[25] showed a closed conformation of the bi-lobed GluN2B ATD architecture[22–25], probably representing the 'allosterically inhibited' functional state. In the presence of agonists, NMDA receptors are known to reside in active states that can trigger ion channel opening, as well as desensitized states with a channel that is closed even in the presence of bound agonists[26]. Despite accumulating structural information on intact NMDA receptors[22,23], as well as isolated ATDs[24,25,27] and LBDs[11,28,29], there is a lack of structures representing the active state and the mechanism of activation has remained unclear. In this study, we present structures of the isolated ATD in the apo-state and of the intact receptor in the activated conformation, providing a detailed mechanistic picture of receptor activation.

Opening of the GluN2B ATD and subunit rearrangement

The only available structures for the heterodimeric NMDA receptor ATDs to date are those bound to allosteric inhibitors ifenprodil and Ro 25-6981, representing the allosterically inhibited state[22–25]. We reasoned that by conducting structural studies without allosteric inhibitors, we could capture the ATD conformation that can activate the NMDA receptor ion channel. Thus, we determined the crystal structure of GluN1–GluN2B ATDs in the absence of an allosteric inhibitor (apo-GluN1b–GluN2B ATD) at 2.9 Å resolution (Extended Data Table 1). We crystallized the purified GluN1b–GluN2B ATD proteins complexed to a Fab fragment derived from mouse monoclonal IgG to improve the quality of the crystals (Extended Data Fig. 2). The crystallographic analysis shows heterodimeric GluN1–GluN2B ATDs that have a bi-lobed architecture composed of the regions previously called R1 and R2 in the structure of GluN1b–GluN2B ATD bound to the allosteric inhibitor ifenprodil[24] (Fig. 1). There are a number of differences between the structures of the apo-GluN1b–GluN2B ATD and the ifenprodil-bound GluN1b–GluN2B ATD[24]. The most apparent difference is the separation of GluN1b R1 and GluN2B R2 in the apo-GluN1b–GluN2B ATD, owing to the ~20° rigid-body opening of the GluN2B ATD bi-lobed structure in the apo-GluN1b–GluN2B ATD compared to that in the ifenprodil–GluN1b–GluN2B ATD (Fig. 1d). This observation is

[1]Cold Spring Harbor Laboratory, W. M. Keck Structural Biology Laboratory, Cold Spring Harbor, New York 11724, USA. [2]Janelia Research Campus, Howard Hughes Medical Institute, Ashburn, Virginia 20147, USA.
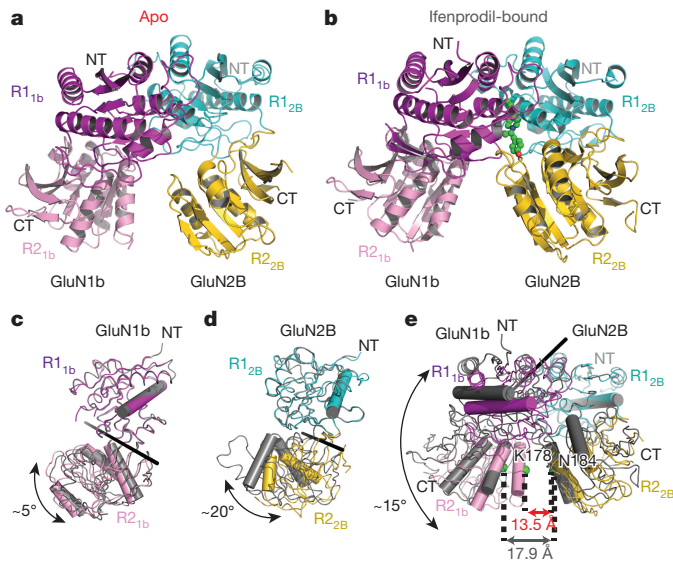
Figure 1 | Structures of GluN1b–GluN2B ATD heterodimers.
a, **b**, Crystal structure of the GluN1b–GluN2B ATD heterodimer in the apo state solved at 2.9 Å (**a**) in comparison with the ifenprodil-bound structure (PDB ID, 3QEL) (**b**). The R1 and R2 lobes are coloured magenta and light pink for GluN1b ATD, and cyan and yellow for GluN2B ATD. Ifenprodil is represented by green spheres. **c**, **d**, Superimposition of the R1 lobes of GluN1b (**c**) and GluN2B (**d**) in the apo and ifenprodil-bound (grey) forms illustrates the relative 'opening' between R1 and R2 lobes. **e**, Superimposing the GluN2B R1 lobes of apo and ifenprodil-bound forms reveals an ~15° rotation of GluN1b ATD relative to GluN2B ATD along the axis of rotation (black rod). The distance of the R2 lobes in the GluN1b–GluN2B heterodimers is measured between GluN1b Lys178 and GluN2B Asn184 (green spheres). CT, C terminal; NT, N terminal.

consistent with previous work suggesting that GluN2B ATD has open-cleft and closed-cleft conformations in the absence and presence of ifenprodil, respectively, on the basis of luminescence resonance energy transfer studies[30]. Another major difference is the rearrangement of the GluN1b and GluN2B subunits involving an ~15° rotation relative to one another (Fig. 1e). This rearrangement brings the lower lobes (R2) of GluN1–GluN2B considerably closer together in the apo-GluN1b–GluN2B ATD compared with the ifenprodil–GluN1b–GluN2B ATD (Fig. 1e, Extended Data Fig. 2c). For example, the distance between the Cα atoms of GluN1b Lys178 and GluN2B Asn184 in apo-GluN1b–GluN2B ATD is 4.4 Å closer than in the ifenprodil–GluN1b–GluN2B ATD (Fig. 1e).

As the subunit arrangement in the apo-GluN1b–GluN2B ATD in our crystal structure is different from that previously observed in the ifenprodil–GluN1b–GluN2B ATD[22], we sought to validate its physiological relevance. Towards this end, we tested whether an inter-subunit disulfide bond can form at the subunit interface observed in the the apo-GluN1b–GluN2B ATD, but not in the ifenprodil–GluN1b–GluN2B ATD in the context of the intact GluN1–GluN2B NMDA receptor by mutating GluN1 and GluN2B residues that are proximal to each other. We expected a spontaneous disulfide bond to form between the mutated cysteines in the intact GluN1–GluN2B NMDA receptor if the subunit interface observed in the crystal structure is physiological. We engineered cysteine residues at GluN1b Phe113 and GluN2B Ala107, and at GluN1b Gly331 and GluN2B Glu75, expressed and purified the mutant GluN1b–GluN2B NMDA receptor in the context of the intact ion channel, and conducted western blot analysis under non-reducing conditions to detect band shifts (Extended Data Fig. 3a). In the two selected positions, the disulfide bonds are formed only when the cysteine mutant (Extended Data Fig. 3) of GluN1 and that of GluN2B are co-expressed and detected by an anti-GluN1 and anti-GluN2B western blot in the absence of
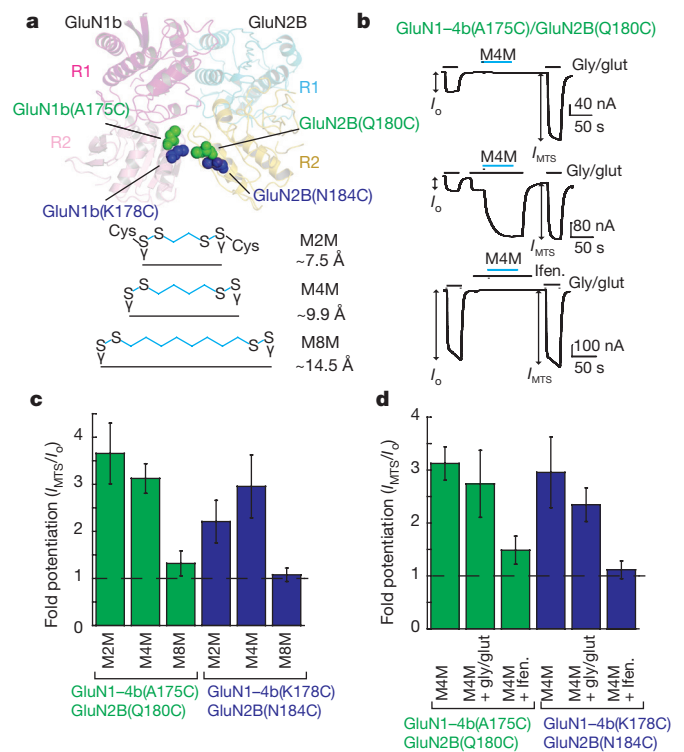

Figure 2 | Conformational trap identifies the apo-GluN1b–GluN2B ATD structure as the 'active' form. a, Location of engineered cysteines in the crystal structure of the apo-GluN1b–GluN2B ATD (GluN1–4b(Ala175Cys)/GluN2B(Gln180Cys)) in green spheres and GluN1–4b(Lys178Cys)/GluN2B(Asn184Cys)) in blue spheres.
b, Application of 200 μM M4M in the presence or absence of 100 μM agonists (glycine and glutamate (gly/glut)) potentiates the macroscopic current measured at the holding potential of −60 mV by two-electrode voltage clamp. No potentiation was observed when M4M was applied in the presence of ifenprodil (ifen.). Shown here are the representative recording profiles for the GluN1–4b(Ala175Cys)/GluN2B(Gln180Cys) pair. **c**, **d**, Fold of potentiation is presented as I_{MTS}/I_o (I, current amplitude) as measured in **b** for bifunctional MTS with different linker lengths (**c**) and M4M applied in different functional states (**d**). Error bars represent ±s.d. for data obtained from at least five different oocytes per experiment.

β-mercaptoethanol. When the cysteine mutants of one subunit is co-expressed with the wild type of the other subunit, no disulfide bonds are formed, indicating that they are specifically formed by the engineered cysteines. Taken together, the above experiments show that the GluN1–GluN2B subunit arrangement observed in the apo-GluN1b–GluN2B ATD crystal structure exists in the context of the intact GluN1b–GluN2B NMDA receptor.

Active conformation of the ATD

To understand the functional state that the crystal structure of the apo-GluN1b–GluN2B ATD may represent, we next attempted to stabilize the conformation observed in the crystal structure and assessed the ion channel activity. We engineered cysteines at the positions in the lower lobes (R2) of the GluN1b and GluN2B ATDs (GluN1b(Ala175Cys)/GluN2B(Gln180Cys) and GluN1b(Lys178Cys)/GluN2B(Asn184Cys)), which face each other and should 'trap' the conformation observed in the crystal structure by tethering the engineered cysteines with bifunctional methanthiosulfonate (bi-MTS) reagents (Fig. 2). The distances between the mutated residues are closer in apo-GluN1b–GluN2B ATD than in ifenprodil–GluN1b–GluN2B ATD as mentioned above (Fig. 1e). When bi-MTS, equal or shorter in length than M4M, binds to the lower lobes of the GluN1b–GluN2B heterodimers, we reasoned that the conformation observed in the apo-GluN1b–GluN2B ATD with the open GluN2B bi-lobed architecture and the rearranged GluN1–GluN2B
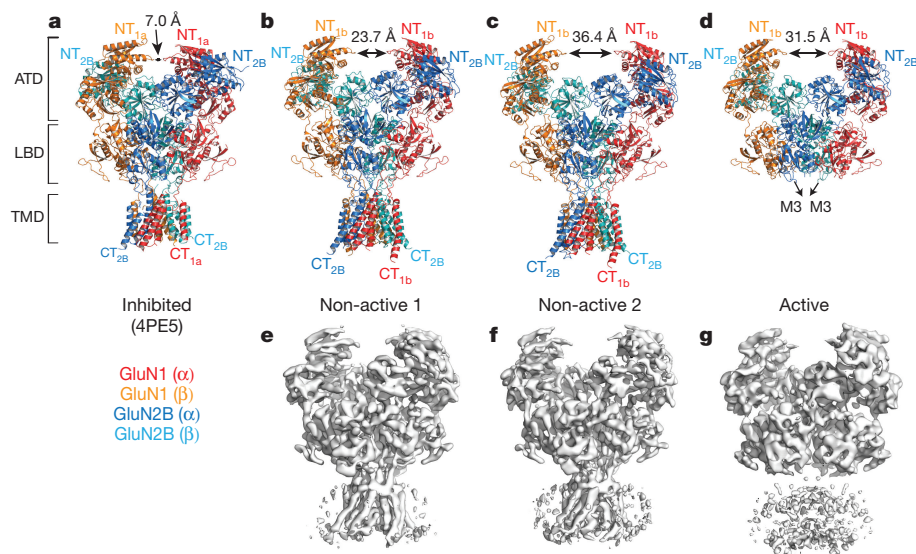
Figure 3 | Overall structures of the intact GluN1–GluN2B NMDA receptors at different conformational states. a, The crystal structure of GluN1a–GluN2B NMDA receptor in complex with glycine, L-glutamate and ifenprodil (PDB ID, 4PE5). **b–d,** Cryo-EM structures of glycine- and L-glutamate-bound GluN1b–GluN2B NMDA receptors classified to reveal different conformations representing the 'non-active' (**b**, **c**) and 'active' (**d**) states. Subunits: red, GluN1 (α); orange, GluN1 (β); blue, GluN2B (α);

cyan, GluN2B (β). The two 'non-active' 3D classes (non-active 1 and 2) have different distances between the two GluN1–GluN2B ATD heterodimers represented as the distance between the $C\alpha$ atoms of Glu320 (299 in GluN1a) of GluN1b (α) and GluN1b (β) (double-sided arrows). The amino and carboxy termini and approximate domain boundaries are indicated. **e–g,** The cryo-EM maps for the 'non-active 1' (**e**), 'non-active 2' (**f**) and 'active' (**g**) states.

subunit orientation should be trapped. To test this, we co-expressed the cysteine mutants of GluN1b and GluN2B in *Xenopus* oocytes and probed the effect of the bi-MTS reagents on the macroscopic current of NMDA receptor by two-electrode voltage clamp. We initialized this experiment by testing bi-MTS with the four-carbon linker (M4M in Fig. 2a) as the estimated distances between the γ-sulfur atom of the mutated cysteines in the GluN1b(Ala175Cys)/GluN2B(Gln180Cys) and GluN1b(Lys178Cys)/GluN2B(Asn184Cys) mutants of apo-GluN1b–GluN2B ATD are ~10 Å and ~9 Å, respectively, roughly matching the length of M4M. The application of M4M to the GluN1b(Ala175Cys)/GluN2B(Gln180Cys) and GluN1b(Lys178Cys)/GluN2B(Asn184Cys) mutants potentiates the NMDA receptor currents by ~3–4-fold (Fig. 2b, c, Extended Data Fig. 4). No such effect is observed when the cysteine mutants of one subunit are co-expressed with the wild type of the other subunit, indicating that the observed functional effect is specific to the engineered cysteines (Fig. 2a and Extended Data Fig. 5a, b). We suggest that this potentiating effect by the bi-MTS conformational trap favoured the NMDA receptor ion channel to reside in the 'active' form. The effect of M4M is observed both in the presence and absence of glycine and glutamate, indicating that conformational alteration in the ATD is independent of agonist binding in the LBD. Furthermore, the potentiation effect was also observed when M2M was applied to both of the above mutant pairs, indicating that the GluN1b–GluN2B distance in R2 may move even closer than observed in the crystal structure, consistent with the single-particle electron cryomicroscopy (cryo-EM) structures shown later. By contrast, when adding M8M, a bi-MTS agent that is 4–5 Å longer than the inter-cysteine distances observed in the apo-GluN1b–GluN2B ATD, no potentiating effect was observed, supporting the view that the distance between the R2 lobes of GluN1b–GluN2B must be reduced during activation (Fig. 2c, Extended Data Fig. 5). Finally, when M4M was applied in the presence of ifenprodil, we observe little or no potentiating effect indicating that it traps the active conformation of GluN1b–GluN2B ATDs but not the inhibited conformation as represented by the crystal structure of the ifenprodil–GluN1b–GluN2B ATD (Fig. 2b, d). Taken together, these experiments indicate that the protein conformation observed in the crystal structure of the apo-GluN1b–GluN2B ATD probably represents the active conformation that facilitates ion channel opening.

Structures of intact GluN1b–GluN2B NMDA receptors

We next investigated how the changes in the GluN1–GluN2B ATD conformation alter subunit arrangement and inter-ATD–LBD interactions to ultimately mediate gating of the ion channel. To answer this, we determined cryo-EM structures of the intact heterotetrameric rat GluN1b–GluN2B NMDA receptor ion channel in the presence of glycine and L-glutamate and in the absence of ifenprodil. The cryo-EM structures were reconstructed at resolutions better than 7 Å and revealed clear secondary structure elements (Fig. 3, Extended Data Figs 6, 7 and Extended Data Table 2). The cryo-EM structures show conservation of general features observed in the recent full-length NMDA receptor crystal structures, including a dimer of GluN1–GluN2B heterodimers arrangement at the ATD and LBD layers, the domain swap between the ATD and LBD, and pseudo-four-fold symmetrical subunit arrangement at the TMD[22,23]. Importantly, three-dimensional (3D) classification of the cryo-EM data revealed different conformational states present in the data set (Fig. 3). Overall, there are roughly three distinct conformations, which we define as 'non-active 1', 'non-active 2', and 'active' (Fig. 3). When compared to the crystal structure of the intact NMDA receptors bound to ifenprodil, glycine and L-glutamate[22,23], which represent the allosterically inhibited functional state, all of the 3D classes contain a GluN2B ATD open bi-lobed architecture, with an ~14°–21° opening similar to the crystal structure of the apo-GluN1b–GluN2B ATD. This opening of the GluN2B ATD increases the distance between the two GluN1 ATDs by as much as ~29 Å in the intact NMDA receptor compared to the ifenprodil-bound form (Fig. 3). The comparison shows that, upon ifenprodil binding, the R1 lobe moves relative to the LBD and TMD to close the bi-lobed architecture of the GluN2B ATD, as well as the gap between the two GluN1 ATDs to inhibit receptor activity.

The two 3D classes, non-active 1 and non-active 2, are both in the state where agonists are bound to the LBD but the ion channel is closed. When focusing on the ATD, both non-active 1 and non-active 2 do not display the ~15° rotation of the GluN1b and GluN2B subunits relative to one another as observed in the crystal structure of the apo-GluN1b–GluN2B ATD, which represents a conformation that can activate the receptor. The arrangements of the dimer of the GluN1b–GluN2B ATD
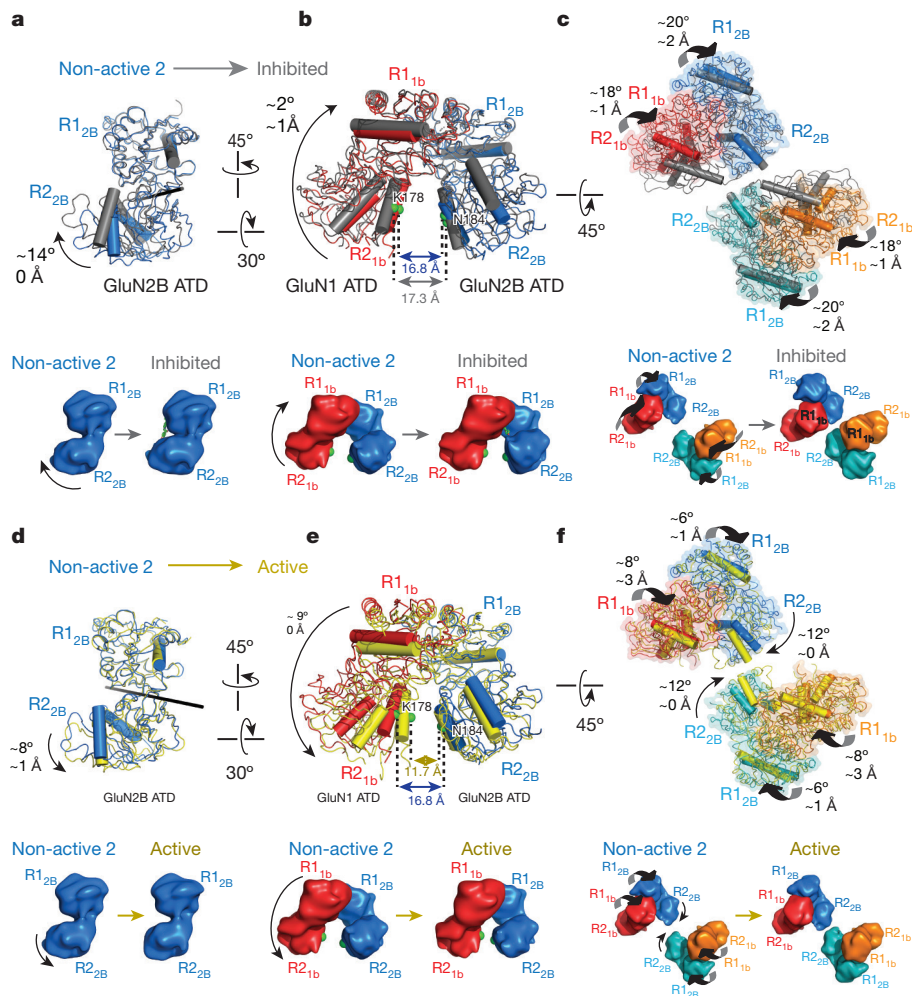
Figure 4 | Changes in conformation and heterotetrameric subunit arrangement in the ATD during ifenprodil inhibition and receptor activation. a–f, Comparison of 3D classes show movements (arrowed arcs) of the bi-lobed architecture in the GluN2B ATD (**a, d**), and rearrangement of the GluN1b–GluN2B ATD heterodimer (**b, e**) and heterotetramer (**c, f**) during transition from the agonist-bound 'non-active 2' conformation (same colour code as in Fig. 3) to the ifenprodil-bound 'inhibited' conformation (PDB ID, 4PE5) (grey) (**a–c**) or to the 'active' conformation

(yellow) (**d–f**). Schematic diagrams are shown below each panel. **a, d,** Superimposition of GluN2B ATD R1 lobes show relative movement of R2 (around black rods) (**a, d**) and rearrangement in the pattern of subunit arrangement (**b, e**) in different functional states. **c, f,** GluN1b–GluN2B ATD heterotetramer from different 3D classes are compared by aligning the centres of masses (COMs) of the ATD heterotetramer, LBD heterotetramer and individual LBDs. Ifenprodil shown as green sticks.

dimers (Fig. 4c), as well as the dimer of GluN1b–GluN2B LBD dimers (Fig. 5a, c, e) are similar to those observed in the crystal structure of the intact NMDA receptor ('inhibited' conformation) (Figs 4 and 5). Consequently, the ion channel pores at the TMD remain closed, confirming that both cryo-EM classes probably represent non-gating or 'non-active' conformations. The difference in non-active 1 and non-active 2 is the extent of bi-lobe opening in the GluN2B ATD, where non-active 2 has an ~7° more open conformation resulting in ~13 Å larger separation between the GluN1 ATDs (Fig. 3). Even though we tentatively call these two conformations 'non-active', it remains uncertain whether they represent functional states equivalent to the 'pre-open' state observed in non-NMDA receptors[17,31] or a 'desensitized' state.
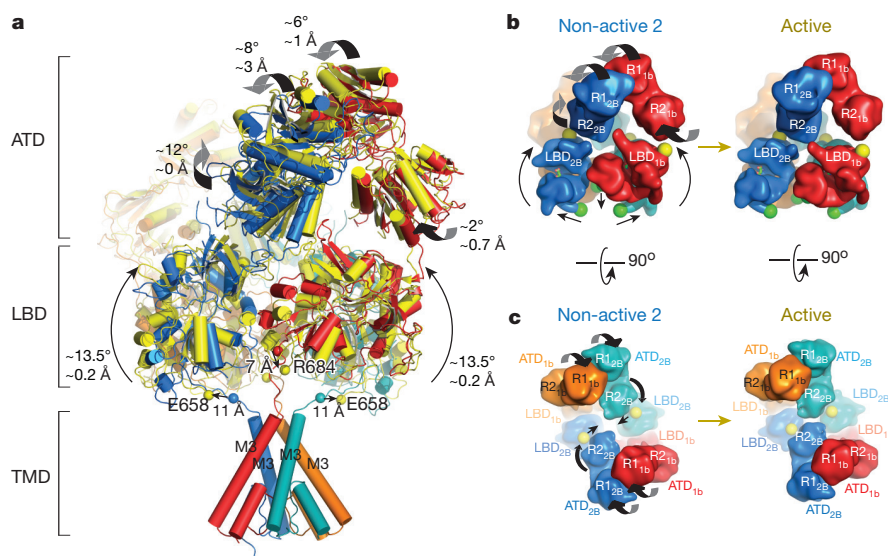
Active conformation

One of the cryo-EM classes, 'active' (Fig. 3), shows the cleft of the bi-lobed GluN2B ATD architecture opened by ~22° and a GluN1b–GluN2B heterodimeric subunit rotated by ~12°, compared to the ifenprodil-bound intact NMDA receptors, which is notably similar to the apo-GluN1b–GluN2B ATD crystal structure representing the active ATD conformation (Figs 1 and 4e and Extended Data Fig. 7). In the heterotetrameric NMDA receptor, the GluN1b–GluN2B

heterodimer pairs rotate by ~12° in opposite directions (Fig. 4f). Importantly, this 3D structure of the active conformation of the ATD also shows large differences in the subunit arrangement of LBDs compared to the other 3D classes representing 'non-active' ATDs, and is also different from the recent crystal structures of the glycine, L-glutamate and ifenprodil complexes[22,23]. Specifically, when transitioning from the non-active 2 to active conformation, the two pairs of GluN1b–GluN2B LBD heterodimers rotate by ~13.5° (Fig. 5b, d, f). These subunit movements in the LBD cause movement of the residues at the LBD–TMD linkers (Fig. 5). For example, when focusing on the residues located right above the pore formed by the M3 TMD helices (Fig. 6a), the consorted movement between the ATD and LBD going from non-active 2 to active described above causes a vertical movement of GluN1b Arg684 and the lateral separation of GluN2B Glu658 by 7 Å and 11 Å, respectively, to dilate the gating ring, a movement that is likely to lead to ion channel gating[32] (Figs 5d, f and 6, Supplementary Videos 1 and 2). Thus, this cryo-EM class is structurally and functionally consistent with an 'active' conformation for GluN1–GluN2B NMDA receptors. Although there is clear density for most of the domains in the active conformation of the receptor, the density for the TMD is not resolved in sufficient detail to directly observe opening of the ion channel, as is the case
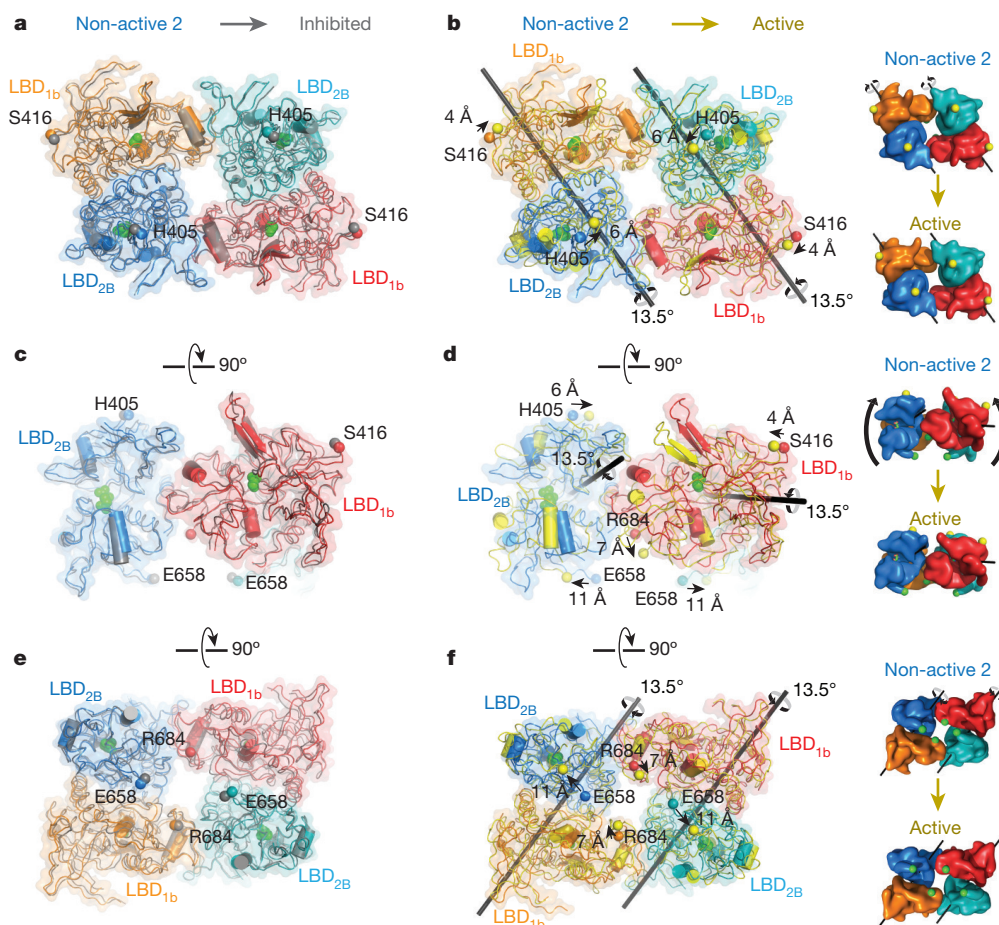
Figure 5 | Conformational changes at the LBD during ifenprodil inhibition and receptor activation. a–f, The same superimposition as in Fig. 4c, f showing the LBD tetramers in the 'non-active 2' (same colour code as in Fig. 3), the 'inhibited' (grey) (**a, c, e**) and the 'active' (yellow) states (**b, d, f**) viewed from the ATD (**a, b**), side (**c, d**) and TMD (**e, f**). The LBD heterodimers rotates (around black rods) during transition from

non-active 2 to active, whereas little or no change occurs between non-active 2 and inhibited. Cα atoms of the residues at the ATD–LBD linker (GluN1b His405 and GluN2B Ser416) and the LBD–TMD linker (GluN1b Arg 684 and GluN2B Glu 658) are shown as spheres. Glycine and L-glutamate at the cleft of the LBD bi-lobes are shown as green spheres. Schematic diagrams are shown to the right of each panel.

Figure 6 | Consorted movement of the ATD and LBD opens the gate. a, Structural comparison of NMDA receptors in the 'non-active 2' (same colour code as in Fig. 3) and the 'active' (yellow) conformations, as in Figs 4 and 5. The M1 and M4 helices of the TMD are omitted for clarity. The arrowed arcs indicate rotation from non-active 2 to active. The first ordered residues on the linker between the M3 helices on the TMD and

LBD in the active structure (GluN1b Arg684 and GluN2B Glu658) are shown as spheres. **b, c**, Schematic diagram viewed from the side of the tetramer (**b**) and top of the ATD (**c**). GluN1b Arg684 and GluN2B Glu658 are shown as green spheres and the residues at the ATD–LBD linker (GluN1b Ser416 and GluN2B His405) are shown as yellow spheres.

for the AMPA receptors[17]. This may indicate that the TMD domain is structurally more variable in activated receptors compared to non-active receptors. Finally, the comparison of the cryo-EM classes with GluA2 AMPA receptor in the pre-open state, which represents a closed channel[17,31], shows that there is a greater difference between the active and pre-open states than between the non-active 2 and pre-open states (Extended Data Fig. 8), consistent with our observation that the TMD ion channel in the non-active structures are also closed.

Conclusion

We report conformational changes in multiple domains that are experimentally linked to activation of mammalian GluN1b–GluN2B NMDA receptors. The activation requires opening of the bi-lobed architecture of the GluN2B ATD and reorientation of the heterodimeric arrangement in the GluN1b–GluN2B ATD, as captured at high-resolution by the crystal structure presented here. These changes lead to rotated GluN1b–GluN2B heterodimeric pairs in both the ATD and LBD, causing dilation of the gating ring. The mechanistic understanding gained in the current study represents an important first step in understanding the sophisticated activation schemes[26,33,34] that are essential for mammalian NMDA receptor function.

1. Traynelis, S. F. *et al.* Glutamate receptor ion channels: structure, regulation, and function. *Pharmacol. Rev.* **62**, 405–496 (2010).
2. Benveniste, M. & Mayer, M. L. Structure-activity analysis of binding kinetics for NMDA receptor competitive antagonists: the influence of conformational restriction. *Br. J. Pharmacol.* **104**, 207–221 (1991).
3. Clements, J. D. & Westbrook, G. L. Activation kinetics reveal the number of glutamate and glycine binding sites on the *N*-methyl-D-aspartate receptor. *Neuron* **7**, 605–613 (1991).
4. Johnson, J. W. & Ascher, P. Glycine potentiates the NMDA response in cultured mouse brain neurons. *Nature* **325**, 529–531 (1987).
5. Nowak, L., Bregestovski, P., Ascher, P., Herbet, A. & Prochiantz, A. Magnesium gates glutamate-activated channels in mouse central neurones. *Nature* **307**, 462–465 (1984).
6. Mayer, M. L., Westbrook, G. L. & Guthrie, P. B. Voltage-dependent block by Mg^{2+} of NMDA responses in spinal cord neurones. *Nature* **309**, 261–263 (1984).
7. Mayer, M. L., MacDermott, A. B., Westbrook, G. L., Smith, S. J. & Barker, J. L. Agonist- and voltage-gated calcium entry in cultured mouse spinal cord neurons under voltage clamp measured using arsenazo III. *J. Neurosci.* **7**, 3230–3244 (1987).
8. Granger, A. J. & Nicoll, R. A. Expression mechanisms underlying long-term potentiation: a postsynaptic view, 10 years on. *Phil. Trans. R. Soc. Lond. B* **369**, 20130136 (2014).
9. Paoletti, P., Bellone, C. & Zhou, Q. NMDA receptor subunit diversity: impact on receptor properties, synaptic plasticity and disease. *Nature Rev. Neurosci.* **14**, 383–400 (2013).
10. Armstrong, N., Sun, Y., Chen, G. Q. & Gouaux, E. Structure of a glutamate-receptor ligand-binding core in complex with kainate. *Nature* **395**, 913–917 (1998).
11. Furukawa, H., Singh, S. K., Mancusso, R. & Gouaux, E. Subunit arrangement and function in NMDA receptors. *Nature* **438**, 185–192 (2005).
12. Mayer, M. L. Crystal structures of the GluR5 and GluR6 ligand binding cores: molecular mechanisms underlying kainate receptor selectivity. *Neuron* **45**, 539–552 (2005).
13. Hansen, K. B., Furukawa, H. & Traynelis, S. F. Control of assembly and function of glutamate receptors by the amino-terminal domain. *Mol. Pharmacol.* **78**, 535–549 (2010).
14. Gielen, M., Siegler Retchless, B., Mony, L., Johnson, J. W. & Paoletti, P. Mechanism of differential control of NMDA receptor activity by NR2 subunits. *Nature* **459**, 703–707 (2009).
15. Yuan, H., Hansen, K. B., Vance, K. M., Ogden, K. K. & Traynelis, S. F. Control of NMDA receptor function by the NR2 subunit amino-terminal domain. *J. Neurosci.* **29**, 12045–12058 (2009).
16. Zhu, S. & Paoletti, P. Allosteric modulators of NMDA receptors: multiple sites and mechanisms. *Curr. Opin. Pharmacol.* **20**, 14–23 (2015).
17. Meyerson, J. R. *et al.* Structural mechanism of glutamate receptor activation and desensitization. *Nature* **514**, 328–334 (2014).
18. Karakas, E., Regan, M. C. & Furukawa, H. Emerging structural insights into the function of ionotropic glutamate receptors. *Trends Biochem. Sci.* **40**, 328–337 (2015).
19. Regan, M. C., Romero-Hernandez, A. & Furukawa, H. A structural biology perspective on NMDA receptor pharmacology and function. *Curr. Opin. Struct. Biol.* **33**, 68–75 (2015).
20. Sobolevsky, A. I., Rosconi, M. P. & Gouaux, E. X-ray structure, symmetry and mechanism of an AMPA-subtype glutamate receptor. *Nature* **462**, 745–756 (2009).
21. Kumar, J., Schuck, P. & Mayer, M. L. Structure and assembly mechanism for heteromeric kainate receptors. *Neuron* **71**, 319–331 (2011).
22. Karakas, E. & Furukawa, H. Crystal structure of a heterotetrameric NMDA receptor ion channel. *Science* **344**, 992–997 (2014).
23. Lee, C. H. *et al.* NMDA receptor structures reveal subunit arrangement and pore architecture. *Nature* **511**, 191–197 (2014).
24. Karakas, E., Simorowski, N. & Furukawa, H. Subunit arrangement and phenylethanolamine binding in GluN1/GluN2B NMDA receptors. *Nature* **475**, 249–253 (2011).
25. Karakas, E., Simorowski, N. & Furukawa, H. Structure of the zinc-bound amino-terminal domain of the NMDA receptor NR2B subunit. *EMBO J.* **28**, 3910–3920 (2009).
26. Banke, T. G. & Traynelis, S. F. Activation of NR1/NR2B NMDA receptors. *Nature Neurosci.* **6**, 144–152 (2003).
27. Farina, A. N. *et al.* Separation of domain contacts is required for heterotetrameric assembly of functional NMDA receptors. *J. Neurosci.* **31**, 3565–3579 (2011).
28. Jespersen, A., Tajima, N., Fernandez-Cuervo, G., Garnier-Amblard, E. C. & Furukawa, H. Structural insights into competitive antagonism in NMDA receptors. *Neuron* **81**, 366–378 (2014).
29. Vance, K. M., Simorowski, N., Traynelis, S. F. & Furukawa, H. Ligand-specific deactivation time course of GluN1/GluN2D NMDA receptors. *Nature Commun.* **2**, 294 (2011).
30. Sirrieh, R. E., MacLean, D. M. & Jayaraman, V. A. Conserved structural mechanism of NMDA receptor inhibition: A comparison of ifenprodil and zinc. *J. Gen. Physiol.* **146**, 173–181 (2015).
31. Dürr, K. L. *et al.* Structure and Dynamics of AMPA Receptor GluA2 in Resting, Pre-Open, and Desensitized States. *Cell* **158**, 778–792 (2014).
32. Kazi, R., Dai, J., Sweeney, C., Zhou, H. X. & Wollmuth, L. P. Mechanical coupling maintains the fidelity of NMDA receptor-mediated currents. *Nature Neurosci.* **17**, 914–922 (2014).
33. Popescu, G. & Auerbach, A. The NMDA receptor gating machine: lessons from single channels. *Neuroscientist* **10**, 192–198 (2004).
34. Popescu, G., Robert, A., Howe, J. R. & Auerbach, A. Reaction mechanism determines NMDA receptor response to repetitive stimulation. *Nature* **430**, 790–793 (2004).

METHODS

Data reporting. No statistical methods were used to predetermine sample size. The experiments were not randomized and the investigators were not blinded to outcome assessment.

Production of GluN1b/GluN2B ATD, GluN1b/GluN2B NMDA receptors and Fab fragment. The constructs of GluN1b and GluN2B ATDs are identical to those used in our previous study, and were expressed and purified in the same way[24]. The purified protein was deglycosylated by endoglycosidase F1. Monoclonal antibodies (mouse IgG) that bind rat GluN2B ATD were obtained by immunizing mice with the purified intact GluN1–GluN2B NMDA receptors using the standard protocol. IgGs were purified from hybridoma cell culture supernatant by Protein-A Sepharose (GE healthcare). Fab fragments of the antibody were obtained by papain proteolysis followed by re-chromatographing onto Protein-A Sepharose to remove the Fc region. The purified GluN1b–GluN2B ATD and Fab were mixed, and the ATD–Fab complex was isolated by Superdex200 (10/300; GE Healthcare). The intact tetrameric GluN1b–GluN2B NMDA receptors were expressed and purified as previously described[22].

Crystallization, data collection and structural determination of apo-GluN1b–GluN2B ATD. The purified GluN1b–GluN2B ATD–Fab complex was concentrated to 8 mg ml^{-1} and dialysed against a buffer containing 10 mM Tris-HCl (pH 8.0) and 50 mM NaCl. The crystals were grown at 18 °C by the hanging-drop vapour diffusion method. GluN1b–GluN2B ATD–Fab complex was mixed with a half volume of reservoir solution (3–5 μl total drop size), which contained 0.1 M sodium acetate (pH 4.5), 27% PEG3350, 2.2 M sodium formate, and 0.05 M calcium chloride. Cryoprotection was achieved by supplying 8% glycerol to the crystallization condition. Crystals were flash-frozen in liquid nitrogen. Data sets were collected at the wavelength of 1.0 Å and at the 23ID-D beamline in the Advanced Photon System in the Argonne National Laboratory and processed using HKL2000 (ref. 35) (Extended Data Table 1). The crystal structure of GluN1b–GluN2B ATD–Fab17 complex was solved by molecular replacement using the coordinate of GluN1b/GluN2B ATD (PDB ID, 3QEL) and Fab (PDB ID, 1BAF) and by using the program Phaser[36]. The model refinement was performed using the program Phenix[37].

Electrophysiology. GluN1–4b/GluN2B NMDA receptors were expressed by injecting cRNAs at a 1:2 ratio (GluN1:GluN2, w/w) into defolliculated *Xenopus laevis* oocytes (0.05–0.15 ng total per oocyte). After 24–48 h incubation at 18 °C, currents were measured by two-electrode voltage clamp in a solution containing 5 mM HEPES, 100 mM NaCl, 0.3 mM BaCl$_2$ and 10 mM Tricine at pH 6.5 (adjusted with KOH) using agarose-tipped microelectrode (0.4–1.0 MΩ) at the holding potential of −60 mV. Currents were evoked by application of 100 μM glycine and L-glutamate. For MTS experiments, fresh stock of MTS reagents were made and added to the recording buffers at the final concentration of 200 μM. The data were analysed using the program Pulse (HEKA) and the graphs were generated by the program Kaleidagraph (Synergy).

Cysteine crosslinking and western blot. Recombinant wild-type and mutant GluN1–4b/GluN2B NMDA receptors (GluN2B CTD truncated as in Extended Data Fig. 1), were expressed in the *Spodoptera frugiperda* (*Sf*9) baculovirus system as described previously[22]. The infected cell pellets were solubilized in a buffer containing 50 mM HEPES pH 7.3, 200 mM NaCl, 0.5% LMN, and 1 mM PMSF. The GluN1–4b/GluN2B NMDA receptor proteins were purified by Strep-Tactin Sepharose (IBA) and subjected to 7% SDS-polyacrylamide gel electrophoresis in the presence and absence of 100 mM β-mercaptoethanol. The proteins were transferred to nitrocellulose membranes (GE healthcare). The membranes were blocked with 5% milk in a phosphate saline buffer containing 0.05% Tween-20, incubated with mouse monoclonal anti-GluN1 antibody (MAB1586, Millipore) or anti-GluN2B antibody (AB93610, Abcam), followed by horseradish peroxidase (HRP)-conjugated anti-mouse secondary antibodies (GE healthcare). The ECL detection kit (GE healthcare) was used to visualize bands.

Cryo-EM specimen preparation and image acquisition. Purified GluN1b/GluN2B NMDA receptor at 2 mg ml^{-1} was placed on C-flat 1.2/1.3 Cu 400 mesh grids (Protochips), which had previously been subjected to glow discharge for 45 s at 15 mA, and plunge-frozen using an FEI Vitrobot Mark 2 with a 3 s blot time and at relative humidity between 85% and 95%. The data were collected on an FEI Titan Krios microscope operating at 300 kV. 1,204 movies were collected on a Gatan K2 Summit direct electron detector (Gatan, Inc.) in super resolution mode with a pixel size of 0.655 Å per super resolution pixel. Each exposure was 21 s long and recorded as a movie of 70 frames. The exposure per frame as reported by Digital Micrograph (Gatan, Inc.) was ~1.4 e$^-$ per Å^2, which corresponds to an exposure of ~8 electrons per pixel per second on the camera. Videos were recorded at a range of underfocus between ~1.0 μm and ~2.5 μm.

Image processing. Super-resolution movie frames were initially corrected for magnification distortion[38]. The frames were then downsampled by a factor of 2 using Fourier cropping to a pixel size of 1.31 Å, motion-corrected and exposure filtered using Unblur[39] and the microscope CTF was determined using CTFFIND4[40] on motion-corrected but non-exposure filtered movie sums. Around 90,000 particles were picked automatically then verified manually from the aligned movie sums which had been exposure filtered, but not noise restored, resulting in a strong low-pass filter. The picked particles were extracted into 256 × 256 boxes. Initial particle alignment parameters were assigned by a brute force search in Frealign v9[41], sampling every 5° and limiting the resolution to 15 Å using a previously determined structure as a reference. These parameters were further refined and classified into six 3D classes with Frealign. For classes 1, 3 and 6, the highest resolution included in the alignment was 8 Å, for class 4 the highest included resolution was 12 Å, and for class 5 it was 6.5 Å. Class 2 showed only low-resolution features and was discarded. The resulting resolutions as determined by the 0.143 cut-off[42] were 5.0–6.7 Å (Extended Data Fig. 6). Maps were rendered using UCSF Chimera[43], after applying a bfactor of −600 Å^2.

Model building. The GluN1a–GluN2B crystal structure (PDB ID, 4PE5)[22] was docked into the cryo-EM maps followed by rigid-body fitting of the individual ATD R1 and R2 lobes and LBDs of both GluN1 and GluN2B into the cryo-EM maps using Coot[44]. Both the rat GluN1a–GluN2B crystal structure (PDB ID, 4PE5)[22] and *Xenopus* GluN1–GluN2B NMDA receptor (PDB ID, 4TLM)[23] were used to model the TMD. The resulting models were manually modified to fit into the density using Coot[44] and refined against the cryo-EM maps using Phenix real space refinement[45]. Refinement statistics are shown in Extended Data Table 2. Class X and class Y are similar to 'non-active 2'.

35. Otwinowski, Z. & Minor, W. Processing of X-ray diffraction data collected in oscillation mode. *Methods Enzymol.* **276,** 307–326 (1997).
36. McCoy, A. J. *et al.* Phaser crystallographic software. *J. Appl. Cryst.* **40,** 658–674 (2007).
37. Adams, P. D. *et al.* PHENIX: building new software for automated crystallographic structure determination. *Acta Crystallogr. D* **58,** 1948–1954 (2002).
38. Grant, T. & Grigorieff, N. Automatic estimation and correction of anisotropic magnification distortion in electron microscopes. *J. Struct. Biol.* **192,** 204–208 (2015).
39. Grant, T. & Grigorieff, N. Measuring the optimal exposure for single particle cryo-EM using a 2.6 A reconstruction of rotavirus VP6. *eLife* **4,** e06980 (2015).
40. Rohou, A. & Grigorieff, N. CTFFIND4: fast and accurate defocus estimation from electron micrographs. *J. Struct. Biol.* **192,** 216–221 (2015).
41. Lyumkis, D., Brilot, A. F., Theobald, D. L. & Grigorieff, N. Likelihood-based classification of cryo-EM images using FREALIGN. *J. Struct. Biol.* **183,** 377–388 (2013).
42. Rosenthal, P. B. & Henderson, R. Optimal determination of particle orientation, absolute hand, and contrast loss in single-particle electron cryomicroscopy. *J. Mol. Biol.* **333,** 721–745 (2003).
43. Pettersen, E. F. *et al.* UCSF Chimera–a visualization system for exploratory research and analysis. *J. Comput. Chem.* **25,** 1605–1612 (2004).
44. Emsley, P., Lohkamp, B., Scott, W. G. & Cowtan, K. Features and development of Coot. *Acta Crystallogr. D* **66,** 486–501 (2010).
45. Afonine, P. V., Headd, J. J., Terwilliger, T. C. & Adams, P. D. New tool: phenix.real_space_refine. *Computational Crystallography Newsletter* **4,** 43–44 (2013).
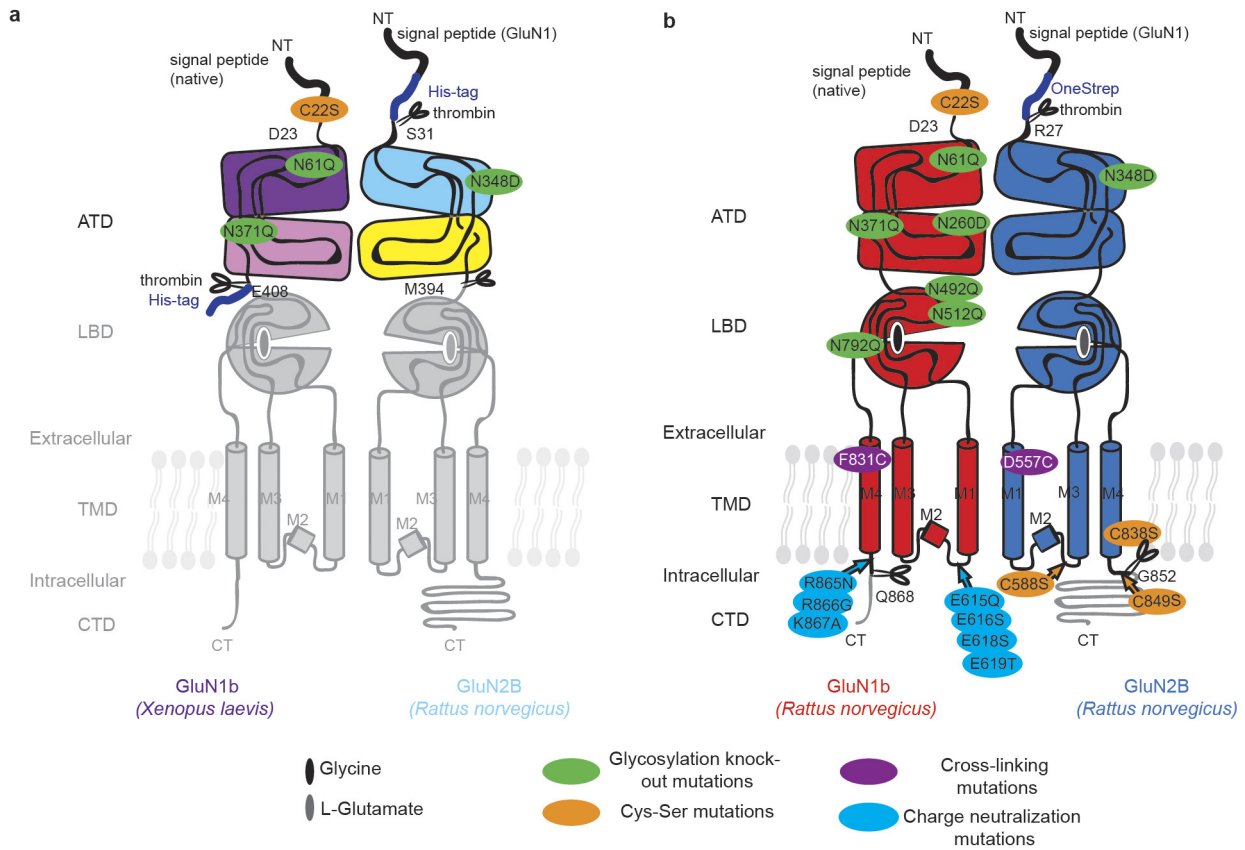
Extended Data Figure 1 | Domain organization and constructs.
**a**, The construct design for GluN1b and GluN2B ATD used in this study. GluN1b from *Xenopus laevis* is combined with GluN2B from rat, as in the previous study on the ATD[24]. **b**, The construct design for the intact GluN1b/GluN2B NMDA receptors from rat. A similar construct was used in previous studies and shown to be fully functional[22].
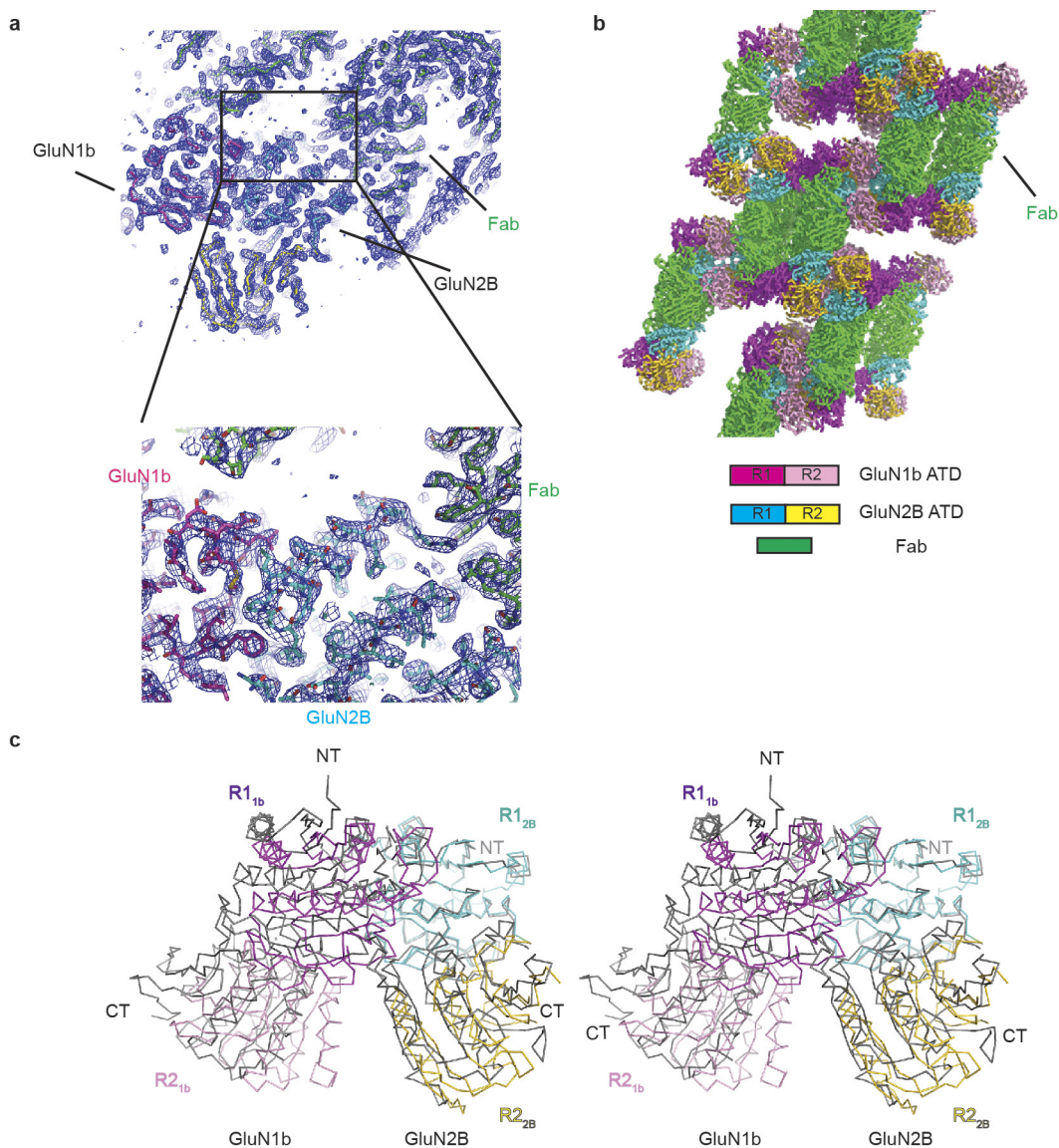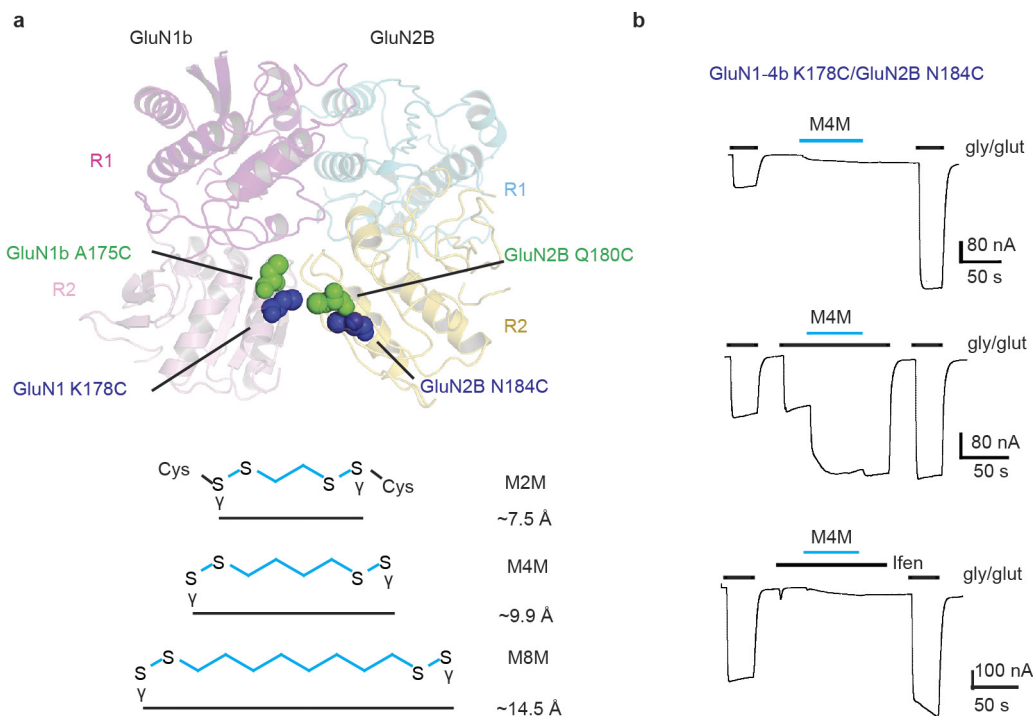
Extended Data Figure 2 | Structure of the apo-GluN1b–GluN2B ATD.
a, Representative $2F_o - F_c$ electron density map contoured at 1.2σ showing continuous density throughout GluN1b, GluN2B and Fab. The quality of the electron density map is at a sufficient level to model amino acid side chains (see lower panel). **b**, Crystal packing of GluN1b–GluN2B ATD–Fab showing that the packing is mediated robustly by Fab molecules (green).

The colour coding for the ATD is the same as in Fig. 1. **c**, Comparison of the apo-GluN1b–GluN2B ATD and ifenprodil–GluN1b–GluN2B ATD (grey) by stereo presentation. Colour coding for the apo-GluN1b–GluN2B ATD is the same as in Fig. 1. Here the two structures are superimposed at GluN2B R1.
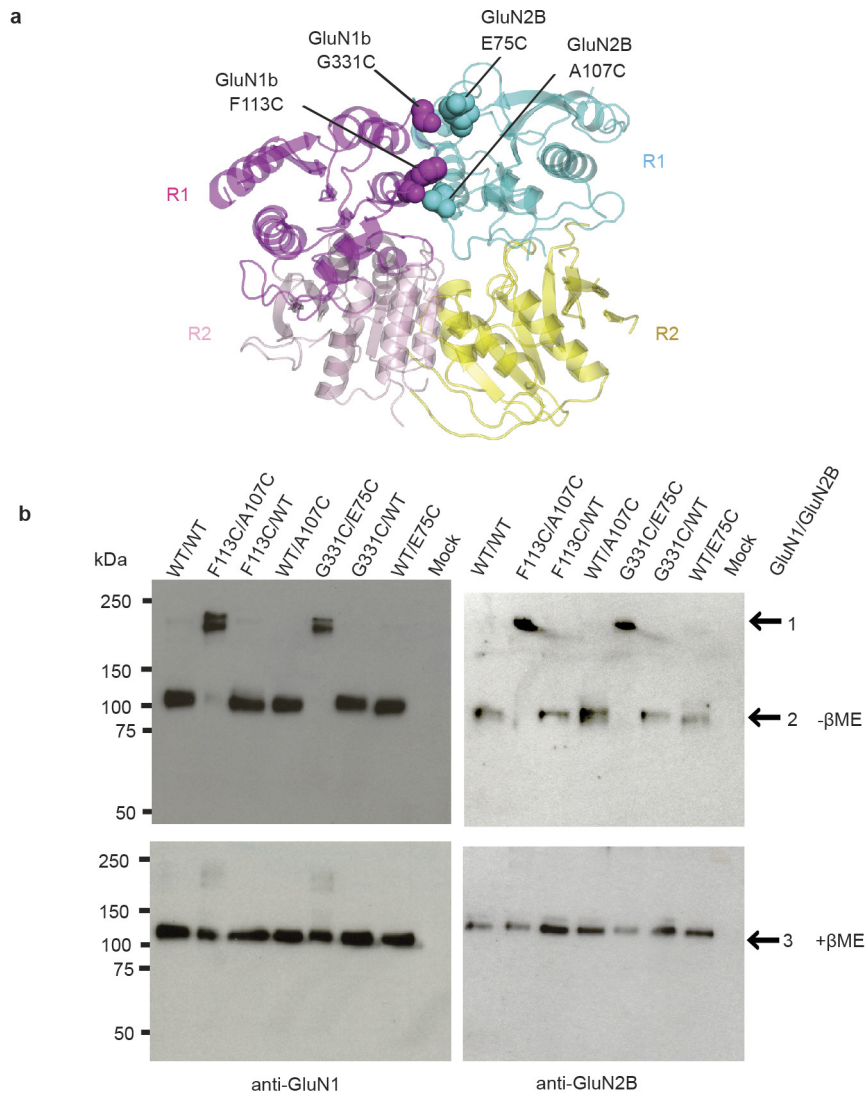
Extended Data Figure 3 | Validation of the crystal structure by disulfide cross-linking. a, Crystal structure of the apo-GluN1b–GluN2B ATD showing locations of the mutated residues, GluN1b Phe113, GluN1b Gly331, GluN2B Ala107 and GluN2B Glu75 in spheres. **b**, Western blots using anti-GluN1 (left) and anti-GluN2B (right) antibodies on purified intact GluN1b/GluN2B NMDA receptor that lacks the CTD.

Upper and lower panels are blots run in the absence and presence of β-mercaptoethanol (βME), respectively. Bands highlighted by arrow 1 are consistent with the molecular weight of GluN1–GluN2B heterodimers, whereas those highlighted by arrows 2 and 3 are consistent with the molecular weights of monomers of GluN1–4b and GluN2B.

Extended Data Figure 4 | Conformational trap shows the apo-GluN1b–GluN2B ATD structure to represent 'active' form-II. a, Location of engineered cysteines in the crystal structure of the apo-GluN1b–GluN2B ATD. The cysteine mutant pairs, GluN1–4b(Ala175Cys)/GluN2B(Gln180Cys) (green spheres) and GluN1–4b(Lys178Cys)/GluN2B(Asn184Cys) (blue spheres) are co-expressed in *Xenopus* oocytes and cross-linked by bifunctional MTS with different linker lengths (M2M, M4M and M8M).

**b**, Application of 200 μM M4M in the presence or absence of 100 μM agonists (glycine (gly)/glutamate (glut)) potentiates the macroscopic current measured at the holding potential of −60 mV by two-electrode voltage clamp. No potentiation was observed when M4M was applied in the presence of ifenprodil (ifen). Shown here are the representative recording profiles for the GluN1–4b(Lys178Cys)/GluN2B(Asn184Cys) pair.
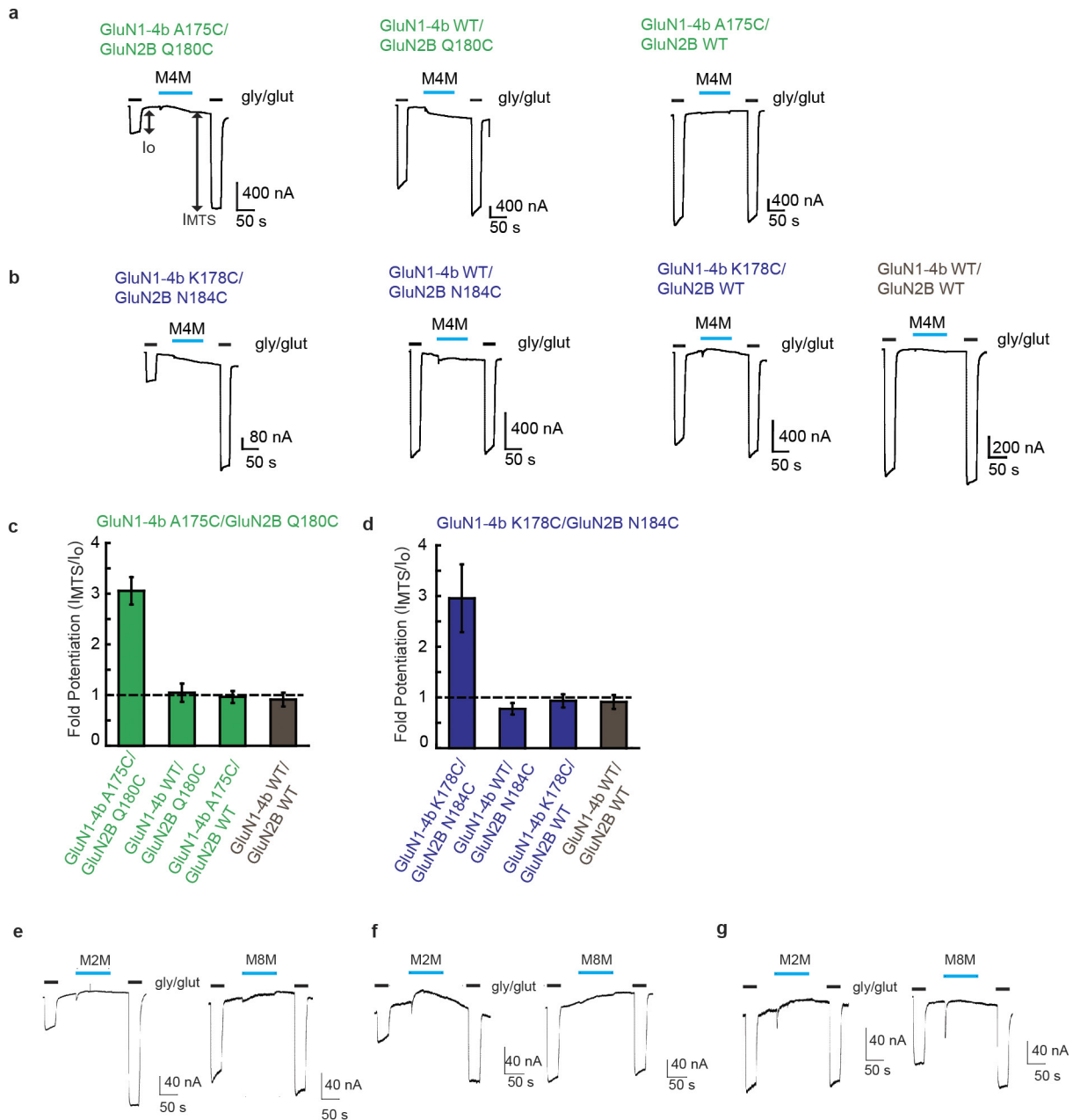
**Extended Data Figure 5 | Effect of bi-MTAs on cysteine mutants.**
a, **b**, M4M specifically traps the active conformation at the engineered cysteines. Representative electrophysiological traces for the mutant pairs, GluN1–4b(Ala175Cys)/GluN2B(Gln180Cys) (green spheres) and GluN1–4b(Lys178Cys)/GluN2B(Asn184Cys) as well as mutant and wild-type pairs. The experiments were conducted by two-electrode voltage clamp as in Fig. 2. The potentiation by M4M (represented by I_{MTS}/I_o) is only observed when both GluN1 and GluN2B cysteine mutants are co-expressed. No potentiation was observed when the cysteine mutant of one subunit is combined with the wild type of the other, indicating that the

effect of M4M modification is specific and validating the relevance of the experiments. **c**, **d**, Bar graphs presenting the degree of potentiation from the recordings in **a** and **b**. Error bars represent ±s.d. for data obtained from five different oocytes per mutant combination. **e**–**g**, M2M but not M8M potentiates the mutant GluN1b–GluN2B NMDA receptor. The same experiment as above or in Fig. 2 was conducted using M2M or M8M on GluN1–4b(Ala175Cys)/GluN2B(Gln180Cys) (**e**) GluN1–4b(Lys178Cys)/ GluN2B(Asn184Cys) (**f**), and wild-type GluN1–4b/GluN2B (**g**). Shown are representative electrophysiological recordings used to estimate the degree of bi-MTS potentiation presented in Fig. 2c.
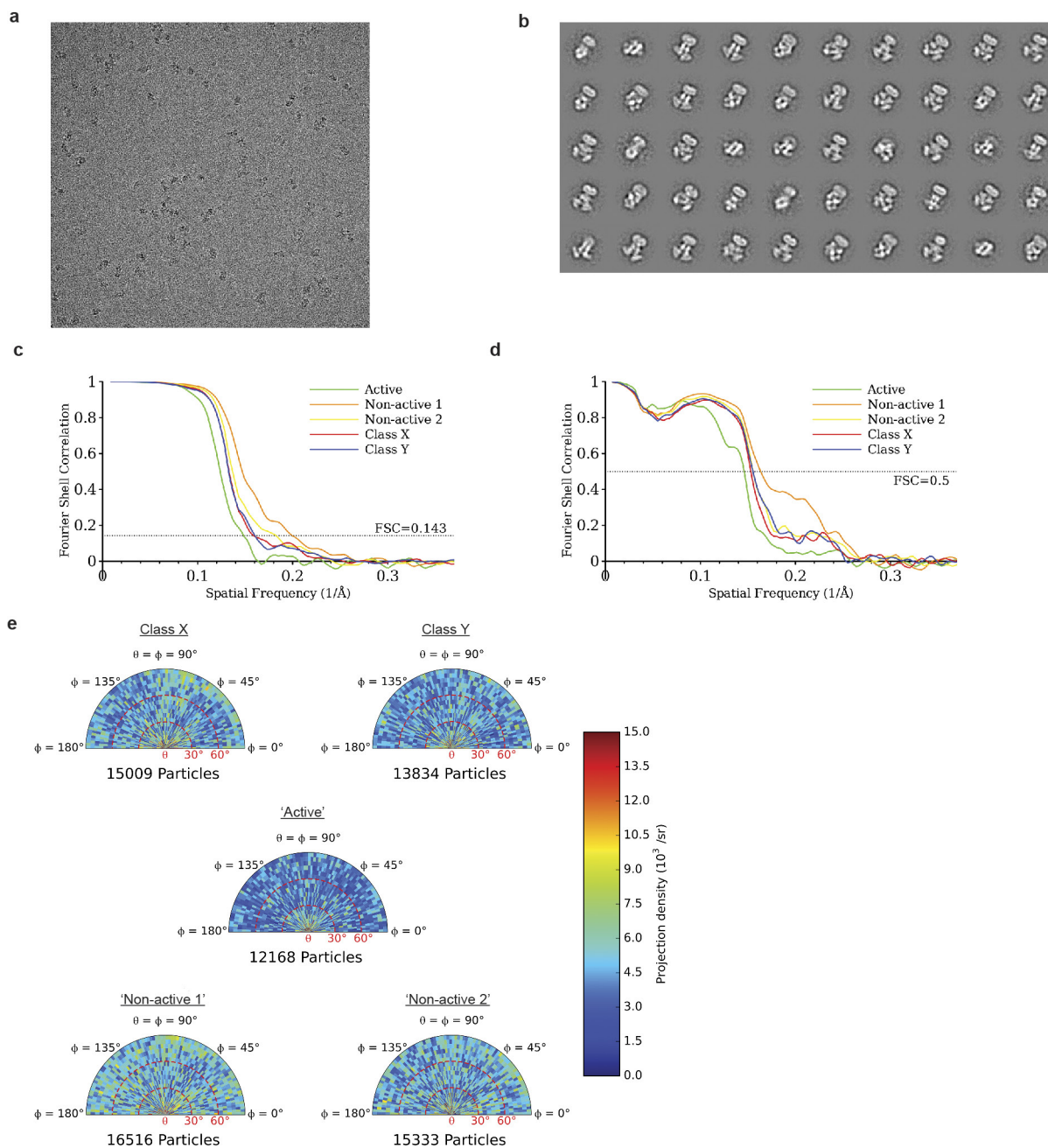
Extended Data Figure 6 | Cryo-EM analysis on GluN1b/GluN2B NMDA receptors. a, Representative motion-corrected image collected at 22,500 magnification. **b**, Two-dimensional class averages. **c**, **d**, Fourier shell correlation curves for unmasked data (**c**) and model versus electron microscopy map (**d**). Class X and Y are similar to 'non-active 2' and were not further analysed. **e**, Orientation plots for each class, plotting the distribution of Euler angles assigned to all particles contributing to that class with an occupancy of at least 80%. For each class, the number of particles which have that class as their highest occupancy value is also shown.
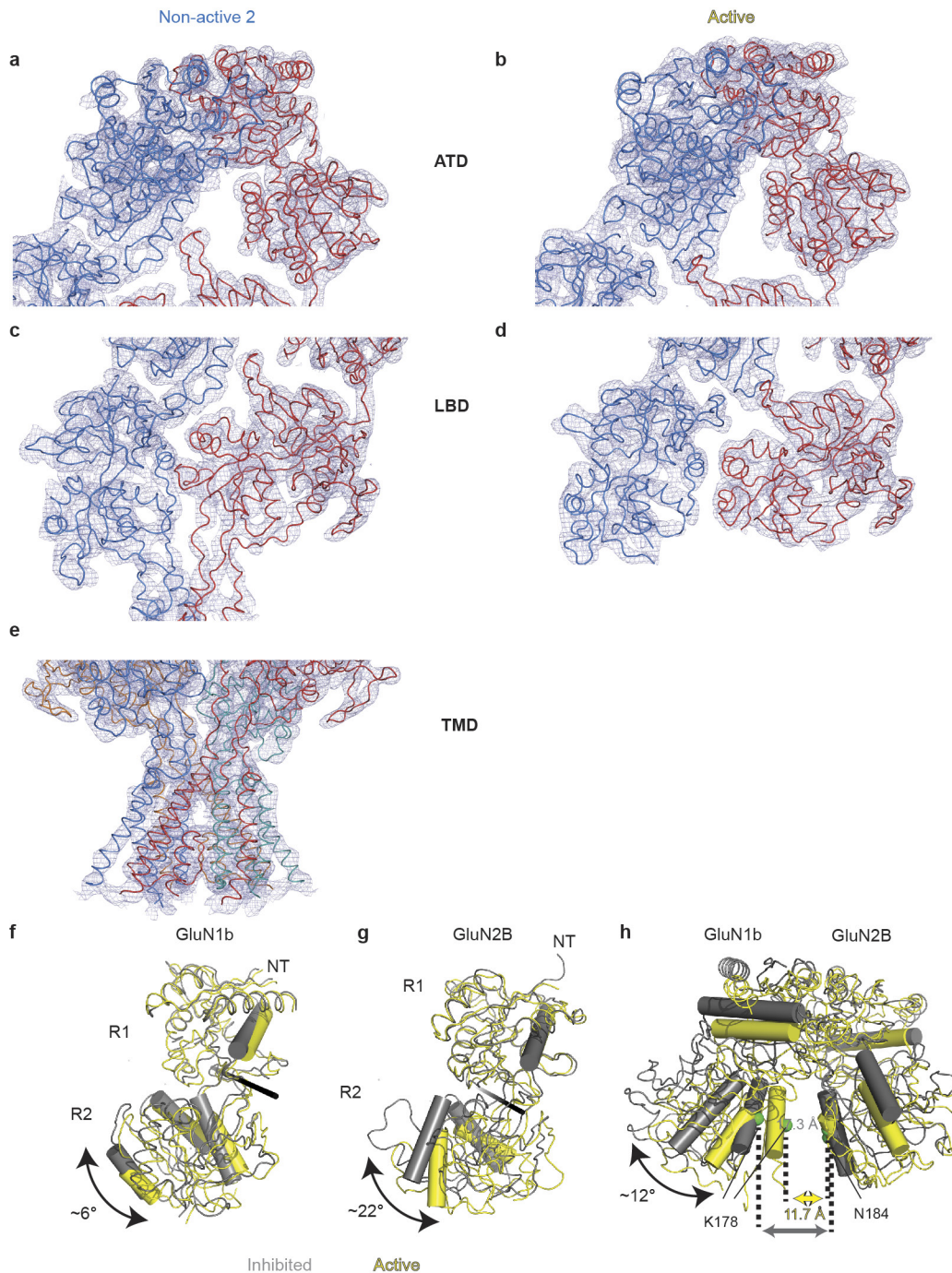
Extended Data Figure 7 | Representative cryo-EM density, model fit and structural comparison of the ATD in inhibited and active conformations of cryo-EM structures. a–e, Here, the cryo-EM maps for non-active 2 and active 3D classes are shown along with the refined models. Densities are shown at the ATD and LBD (**a–d**) for both of the 3D classes and at the TMD (**e**) for non-active 2. **f, g,** Superimposition of R1 lobes of GluN1b (**f**) and GluN2B (**g**) illustrates the relative 'opening' between R1 and R2 lobes in the inhibited and active forms of intact NMDA receptors. The extent of GluN2B ATD opening is similar to that observed between the crystal structures of the ifenprodil–GluN1b–GluN2B ATD and the apo-GluN1b–GluN2B ATD as in Fig. 1. GluN1b and

GluN2B ATDs are shown in grey and yellow for the inhibited and active states, respectively. **h,** Comparison of the GluN1b–GluN2B ATD heterodimers between ifenprodil inhibited and active cryo-EM structures. Superimposition of the GluN2B R1 lobes reveals an ~12° rotation of the GluN1b ATD relative to the GluN2B ATD in the similar manner to the crystal structure of the apo-GluN1b–GluN2B ATD as in Fig. 1. The black rods indicate the axis of rotation between the two cryo-EM structures. The distance of the R2 lobes in the GluN1b–GluN2B heterodimers is measured between Cα atoms of GluN1b(Lys178) and GluN2B(Asn184) (green spheres).
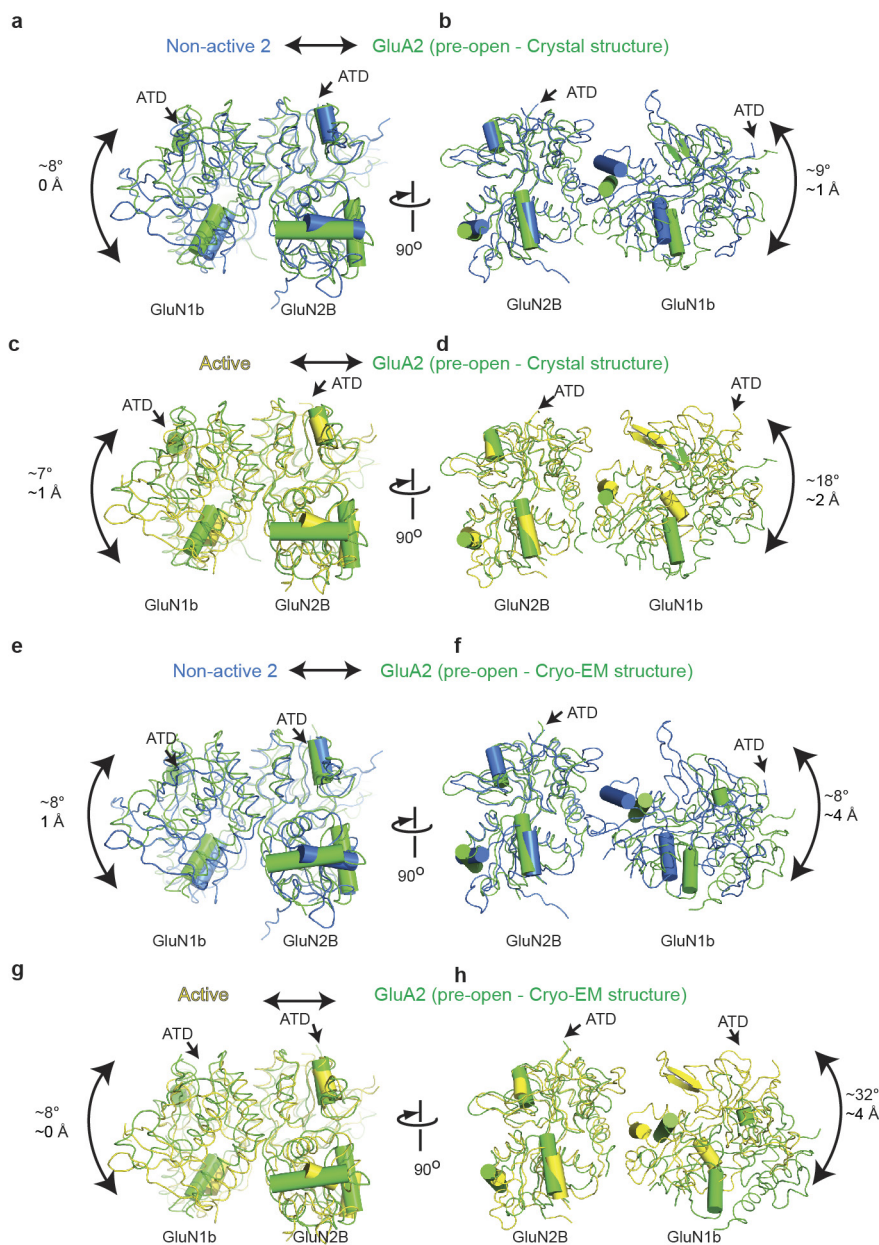
Extended Data Figure 8 | Structural comparison of the GluN1–GluN2B LBD in non-active and active conformations to the GluA2 LBD in pre-open state. a–d, The crystal structure of GluA2 AMPA receptor in the pre-open state (PDB ID, 4U1W; shown in green) aligned with the structures of GluN1–GluN2B in the non-active 2 (blue) (**a, b**) and active conformation (yellow) (**c, d**) by superimposing the LBDs of GluN2B onto GluA2. **e–h,** The equivalent superimposition with the cryo-EM structure of GluA2 AMPA receptor in the pre-open state (PDB ID, 4UQ6; shown in green). The overlaid structures are viewed through the LBD heterodimer interface (**a, c** or **e, g**) and the dimer of heterodimer interface (**b, d** or **f, h**). Here, the GluN2B LBD of the GluN1b–GluN2B NMDA receptor is superimposed onto the LBD of the GluA2 AMPA receptor and the shift of the GluN1 LBD is measured with respect to the other GluA2 LBD. The homodimeric arrangement of GluA2 AMPA receptor in the pre-open state is similar to the heterodimeric arrangements of GluN1b–GluN2B NMDA receptors in both non-active 2 and active states (**a, c** or **e, g**). However, when the dimer of homodimer arrangement of GluA2 AMPA receptor is compared to the dimer of heterodimers arrangement of the GluN1b–GluN2B NMDA receptor, a greater difference is observed for the active NMDA receptor (**d, h**) than for the non-active 2 NMDA receptor (**b, f**). Here, the non-active 2 NMDA receptor as in Fig. 3 is subjected to superimposition. The non-active 1 and non-active 2 NMDA receptors have similar subunit arrangements in the LBD. The numbers in each panel represent degrees of rotations and translations.

Extended Data Table 1 | Data collection and refinement statistics for X-ray crystallography

	Apo-GluN1b/GluN2B ATD − Fab17
Data collection	
Space group	C2
Cell dimensions	
a, b, c (Å)	247.4, 80.0, 181.4
α, β, γ (°)	90.0, 127.2, 90.0
Resolution (Å)	50-2.90(2.93-2.90) *
R_{merge}	0.099 (0.602)
$I/\sigma I$	8.5 (1.84)
Completeness (%)	91.4 (93.0)
Redundancy	4.0 (3.5)
Refinement	
Resolution (Å)	30-2.9
No. reflections	52,910
R_{work}/ R_{free}	0.273/0.302
No. atoms	
Protein	15,899
Ion (Na)	1
Water	112
B-factors	
Protein	46.3
Ligand/ion	52.1
Water	37.9
R.m.s deviations	
Bond lengths (Å)	0.008
Bond angles (º)	1.068

*Highest resolution shell is shown in parentheses.

Extended Data Table 2 | Refinement statistics for the cryo-EM structures

	Active	Non-Active 1	Non-Active 2	Class X	Class Y
PDB ID	5FXG	5FXH	5FXI	5FXJ	5FXK
EMDB ID	EMD-3352	EMD-3353	EMD-3354	EMD-3355	EMD-3356
Refinement					
Resolution (Å)	6.8	6.1	6.4	6.5	6.4
Map to Model CC	0.77	0.79	0.80	0.78	0.80
No. atoms					
Protein	12,693	15,578	15,381	15,475	15,598
R.m.s deviations					
Bond lengths (Å)	0.003	0.006	0.003	0.004	0.005
Bond angles (º)	0.55	0.55	0.60	0.58	0.55
Ramachandran					
Favored (%)	88.3	90.4	90.2	88.0	88.8
Allowed (%)	11.5	9.2	9.4	11.4	10.7
Disallowed (%)	0.2	0.5	0.4	0.6	0.5